

**Ca<sub>3</sub>Pt<sub>4+x</sub>Ge<sub>13-y</sub> and Yb<sub>3</sub>Pt<sub>4</sub>Ge<sub>13</sub>: new derivatives of the Pr<sub>3</sub>Rh<sub>4</sub>Sn<sub>13</sub> structure type**

Roman Gumeniuk,<sup>\*a</sup> Lev Akselrud,<sup>a</sup> Kristina O. Kvashnina,<sup>c</sup> Walter Schnelle,<sup>a</sup> Alexander A. Tsirlin,<sup>a</sup> Caroline Curfs,<sup>c</sup> Helge Rosner,<sup>a</sup> Michael Schöneich,<sup>b</sup> Ulrich Burkhardt,<sup>a</sup> Ulrich Schwarz,<sup>a</sup> Yuri Grin<sup>a</sup> and Andreas Leithe-Jasper<sup>a</sup>

Received 14th February 2012, Accepted 22nd March 2012

DOI: 10.1039/c2dt30339f

The new phases Ca<sub>3</sub>Pt<sub>4+x</sub>Ge<sub>13-y</sub> ( $x = 0.1$ ;  $y = 0.4$ ; space group  $I2_13$ ;  $a = 18.0578(1)$  Å;  $R_1 = 0.063$ ;  $R_p = 0.083$ ) and Yb<sub>3</sub>Pt<sub>4</sub>Ge<sub>13</sub> (space group  $P4_2cm$ ;  $a = 12.7479(1)$  Å;  $c = 9.0009(1)$  Å;  $R_1 = 0.061$ ,  $R_p = 0.117$ ) are obtained by high-pressure, high-temperature synthesis and crystallize in new distortion variants of the Pr<sub>3</sub>Rh<sub>4</sub>Sn<sub>13</sub> type. Yb<sub>3</sub>Pt<sub>4</sub>Ge<sub>13</sub> features Yb in a temperature-independent non-magnetic 4f<sup>14</sup> (Yb<sup>2+</sup>) configuration validated by X-ray absorption spectra and resonant inelastic X-ray scattering data. Ca<sub>3</sub>Pt<sub>4+x</sub>Ge<sub>13-y</sub> is diamagnetic ( $\chi_0 = -5.05 \times 10^{-6}$  emu mol<sup>-1</sup>). The Sommerfeld coefficient  $\gamma = 4.4$  mJ mol<sup>-1</sup> K<sup>-2</sup> for Ca<sub>3</sub>Pt<sub>4+x</sub>Ge<sub>13-y</sub>, indicates metallic properties with a low density of states at the Fermi level in good agreement with electronic structure calculation ( $N(E_F) = 3.3$  eV<sup>-1</sup>/f.u.); the Debye temperature ( $\theta_D$ ) is 398 K.

**Introduction**

Intermetallic compounds with a crystal structure composed of rigid covalently bonded cage-forming frameworks enclosing electropositive metal atoms like rare-earth, actinide or alkaline-earth show a wealth of topical physical phenomena such as valence fluctuations, Kondo behaviour, heavy-fermion properties, superconductivity, thermoelectricity, *etc.*<sup>1-4</sup> To this group of materials belong, in particular, intermetallic clathrates,<sup>5,6</sup> compounds crystallizing in structures derived from the perovskite motif,<sup>7</sup> filled skutterudites<sup>1</sup> and derivatives of the Pr<sub>3</sub>Rh<sub>4</sub>Sn<sub>13</sub> type.<sup>8</sup> Recently, filled skutterudites with a new type of [Pt<sub>4</sub>Ge<sub>12</sub>] framework MPt<sub>4</sub>Ge<sub>12</sub> (with  $M = \text{Sr, Ba, La-Nd, Eu}$ ) were discovered.<sup>9,10</sup> At ambient pressure the formation of filled skutterudites MPt<sub>4</sub>Ge<sub>12</sub> has been observed only for light rare-earth (RE) metals, so that a high-pressure technique was used to synthesize representatives with heavier RE. Application of high-pressure has proven successful for syntheses of phosphorus-based skutterudites<sup>11,12</sup> and SmPt<sub>4</sub>Ge<sub>12</sub>.<sup>13</sup> However, in the samples with nominal composition CaPt<sub>4</sub>Ge<sub>12</sub> and REPt<sub>4</sub>Ge<sub>12</sub> (RE = Gd–Yb) three phases were observed: compounds with a stoichiometry M<sub>3</sub>Pt<sub>4</sub>Ge<sub>13</sub>, MPtGe<sub>2</sub> and free Ge. Cubic symmetry and lattice parameter close to  $\sim 9.5$  Å (deduced from the indexing of only

the strongest reflections) for the phases M<sub>3</sub>Pt<sub>4</sub>Ge<sub>13</sub> suggested resemblance with a Pr<sub>3</sub>Rh<sub>4</sub>Sn<sub>13</sub> type of structure.

This structure type is closely related to skutterudites and features the [Rh<sub>4</sub>Sn<sub>12</sub>] framework with cubooctahedral voids occupied by Pr cations as well as enlarged icosahedral cavities hosting the remaining Sn atoms (see discussion below). Intermetallic compounds with this atomic pattern were found in many systems  $A-T-X$  (where  $A = \text{alkaline-earth, rare-earth or actinide metal}$ ,  $T = \text{transition metal}$  and  $X = \text{In, Si, Ge or Pb}$ ).<sup>14</sup>

They became an object of numerous studies, mostly owing to the interesting interplay between magnetic and superconducting properties.<sup>15-19</sup> Here, it should also be noted that the precise determination of the crystal structure of compounds of this type is difficult. One of the  $X$  atoms, residing in a position at the center of an enlarged regular icosahedral cavity, shows a local positional disorder or a formation of a random mixture of  $A$  and  $X$  or  $T$  and  $X$  elements. This is the case, *e.g.*, in Ce<sub>3</sub>Rh<sub>4</sub>Sn<sub>13</sub><sup>20</sup> and Yb<sub>3</sub>Co<sub>4.3</sub>Sn<sub>12.7</sub>.<sup>18</sup> Some other members of this family crystallize with a doubled body-centered cubic unit cell in the non-centrosymmetric space group  $I4_132$  (*i.e.* La<sub>3</sub>Rh<sub>4</sub>Sn<sub>13</sub><sup>21</sup> and Gd<sub>3</sub>Ir<sub>4</sub>Sn<sub>13</sub><sup>22</sup>). Moreover, in the single crystal X-ray diffraction data for the Pr<sub>3</sub>Rh<sub>4</sub>Sn<sub>13</sub> prototype, Miraglia *et al.*<sup>23</sup> observed superstructure reflections indicating a possible doubling of the unit cell. However, these authors could not completely refine the superstructure due to strong correlation of the refined parameters yielding undefined displacement ellipsoids. Finally, Tm<sub>3</sub>Co<sub>4</sub>Ge<sub>13</sub> adopts a commensurately modulated crystal structure.<sup>24</sup>

In this paper, we report on the preparation, crystal structure and physical properties of two new phases, cubic Ca<sub>3</sub>Pt<sub>4+x</sub>Ge<sub>13-y</sub> and tetragonal Yb<sub>3</sub>Pt<sub>4</sub>Ge<sub>13</sub>, both with crystal structures related to the Pr<sub>3</sub>Rh<sub>4</sub>Sn<sub>13</sub> type.

<sup>a</sup>Max-Planck-Institut für Chemische Physik fester Stoffe, Nöthnitzer Str. 40, 01187 Dresden, Germany. E-mail: gumeniuk@cpfs.mpg.de; Fax: +49 351 4646 4002; Tel: +49 351 4646 4275

<sup>b</sup>Anorganische Chemie, Technische Universität Dresden, 01062 Dresden, Germany

<sup>c</sup>ESRF, 6 rue Jules Horowitz, BP 220, 38043 Grenoble Cedex 9, France

## Result and discussion

### Structure determination

The powder synchrotron X-ray diffraction (XRD) pattern of  $\text{Ca}_3\text{Pt}_{4+x}\text{Ge}_{13-y}$  (161 reflections) was successfully indexed on the basis of a body-centered cubic unit cell with a lattice parameter of  $a = 18.0578(1)$  Å. Analysis of the extinction conditions showed seven possible space groups with diffraction symbols:  $m\bar{3}I$ ---,  $m\bar{3}mI$ --- and  $mmI4$ ---. As the first model for the refinement, the known structure of  $\text{La}_3\text{Rh}_4\text{Sn}_{13}$  (space group  $I4_132$ , diffraction symbol  $m\bar{3}mI4$ ---, reflection conditions  $00l$ ,  $l = 4n$ )<sup>21</sup> was used. This refinement converged with reliability factors  $R_1 = 0.086$ ,  $R_p = 0.101$  and interatomic distances, which were in good agreement with the sum of atomic radii of the elements. However, the calculated intensity of some reflections was substantially lower than the experimentally observed one (inset Fig. 1). The differences cannot be explained by preferential orientation of the sample because the reflections do not belong to a distinct zone(s). This finding indicated that  $\text{Ca}_3\text{Pt}_{4+x}\text{Ge}_{13-y}$  crystallizes most probably in one of the six space groups with diffraction symbols  $m\bar{3}I$ --- or  $m\bar{3}mI$ --- for which reflections  $00l$  with  $l = 4n + 2$  are also expected. However, the assignment of these reflections is ambiguous since in the cubic crystal system, a reflection like  $(0\ 0\ 6)$  can also be indexed as  $(2\ 2\ 4)$ .

Nevertheless, as one can see from Fig. 1, the intensity of the  $(2\ 4\ 4)$  peak is strongly reduced in the structural model with space group  $I4_132$ . The same situation holds for the reflection with index  $(8\ 8\ 14)$ , alternative to  $(0\ 0\ 18)$  (not shown in Fig. 1). These were additional hints in favour of space groups with diffraction symbols  $m\bar{3}I$ --- or  $m\bar{3}mI$ ---. All attempts to find structural models for the new germanide in the centrosymmetric group  $Im\bar{3}m$  as well as non-centrosymmetric groups  $I432$  and

**Table 1** Crystallographic data for  $\text{Ca}_3\text{Pt}_{4+x}\text{Ge}_{13-y}$  and  $\text{Yb}_3\text{Pt}_4\text{Ge}_{13}$  at 293 K

Composition	$\text{Ca}_3\text{Pt}_{4+x}\text{Ge}_{13-y}$ ( $x = 0.1$ ; $y = 0.4$ )	$\text{Yb}_3\text{Pt}_4\text{Ge}_{13}$
Space group	$I2_13$ (no. 199)	$P4_2cm$ (no. 101)
Unit cell parameters		
$a$ (Å)	18.0578(1)	12.7479(1)
$c$ (Å)		9.0009(1)
$V$ (Å <sup>3</sup> )	5888.3(1)	1462.7(1)
Formula units per cell, $Z$	16	4
Calc. density, g cm <sup>-3</sup>	8.256	10.185
Diffraction system	ID 31, ESRF	ID 31, ESRF
Radiation, $\lambda$ (Å)	Synchrotron, 0.39987	Synchrotron, 0.39987
Step size (°2 $\theta$ )	0.001	
$R_1/R_p^a$	0.063/0.083	0.061/0.117

<sup>a</sup>  $R_1 = \sum |I_i^{\text{obs}} - I_i^{\text{calc}}| / \sum |I_i^{\text{obs}}|$ ;  $R_p = \sum w(I_i^{\text{obs}} - I_i^{\text{calc}})^2 / \sum w(I_i^{\text{obs}})^2$ . (Program package WinCSD).

$I4_3m$  failed. The structural model obtained in space group  $Im\bar{3}$  (final values of reliability factors  $R_1 = 0.096$ ,  $R_p = 0.098$ ) is characterized by strong disorder: four crystallographic positions are partially occupied by Ge atoms, whereas two other sites reveal random mixtures of Ge and Pt atoms. Some Ge–Ge distances are shortened by ~13%, Ca–Ge by ~10%, and the final refined composition  $\text{Ca}_3\text{Pt}_{4.2}\text{Ge}_{12.2}$  deviates strongly from the nominal one. To improve this situation, we attempted further symmetry reduction and successfully refined the structure in space group  $I2_13$  as evidenced by significantly lower residuals.

Details of the refinement of the crystal structure of  $\text{Ca}_3\text{Pt}_{4+x}\text{Ge}_{13-y}$  ( $x = 0.1$ ,  $y = 0.4$ ) in space group  $I2_13$  are given in Table 1. Final values of atomic coordinates and displacement parameters together with the shortest interatomic distances are presented in Table 2. The refinement of this structural model provides good agreement between calculated and experimentally observed XRD intensities. In the initial refinement, strongly enhanced (by a factor of 3, compared to other Ge atoms) displacement parameters  $B_{\text{iso}}$  for Ge1 and Ge4 indicated partial occupancy of these sites. On the other hand, the value of the displacement parameter of the atom occupying the  $8a$  site was only  $0.2(1)$  Å<sup>2</sup>. Refinement with a random mixture of Ge and Pt atoms on this position and partial occupation of Ge1 and Ge4 sites leads to reliable values of the isotropic displacement parameters (Table 2). Based on the lowest observed reliability factors (Table 1) as well as reasonable interatomic distances (Table 2) we consider this structural model as the most suitable.

The strongest peaks in the powder XRD pattern of the  $\text{Yb}_3\text{Pt}_4\text{Ge}_{13}$  sample, measured on a HUBER G670 imaging plate Guinier camera, were indexed using a cubic primitive lattice with  $a_{\text{cub}} = 9.0045$  Å (some of them are shown in Fig. 2). The presence of additional weak reflections indicated a doubling of the unit cell. Indeed, all reflections observed in the XRD pattern were indexed with lattice parameter  $a \approx 2a_{\text{cub}} = 18.0091$  Å of a body-centered cubic lattice. However, some peaks in this pattern are either broadened or show pronounced asymmetry (Fig. 2). This fact prompted us to perform a high resolution (HR) synchrotron XRD experiment. A clear splitting of the “broadened” and “asymmetrical” reflections is observed, thus indicating a

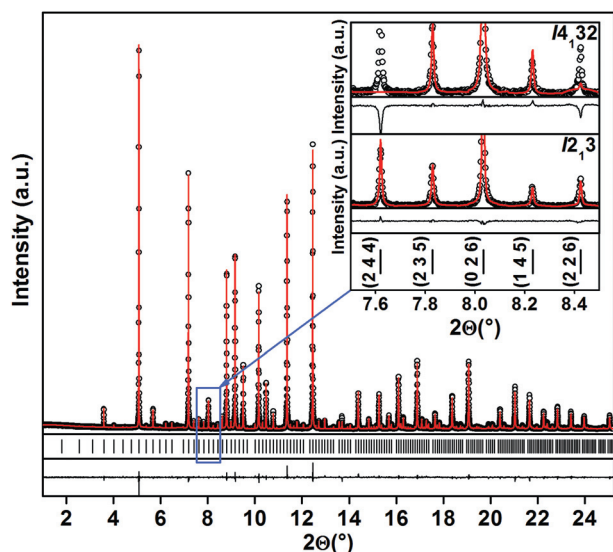


**Fig. 1** Experimental (black circles) and calculated (red line) synchrotron XRD patterns ( $\lambda = 0.39987$  Å) of  $\text{Ca}_3\text{Pt}_{4+x}\text{Ge}_{13-y}$ . The difference plot is shown as a black line in the bottom part. Reflection positions are indicated by ticks. Inset: calculated and measured intensities in space groups  $I4_132$  and  $I2_13$  for reflections in the  $2\theta$  range of  $7.5$ – $8.5^\circ$ .

**Table 2** Atomic coordinates, displacement parameters, and shortest interatomic distances ( $d_{\min}$ , Å) in the crystal structures of  $\text{Ca}_3\text{Pt}_{4+x}\text{Ge}_{13-y}$  and  $\text{Yb}_3\text{Pt}_4\text{Ge}_{13}$ 

$\text{Ca}_3\text{Pt}_{4+x}\text{Ge}_{13-y}$ ( $x = 0.1$ ; $y = 0.4$ )							
Atom	Site	$x$	$y$	$z$	$B_{\text{iso}}(\text{\AA}^2)$	$d_{\min}(\text{\AA})$	CN
Ca1	24c	0.1263(7)	0.2524(9)	0.5009(8)	1.02(2)	–Ge1 – 2.92(1)	16
Ca2	24c	0.0018(8)	0.37190(9)	0.2512(7)	1.02(2)	–Ge8 – 3.01(2)	16
Pt1	8a	0.12241(2)	$x$	$x$	1.15(2)	–3Ge2 – 2.474(6)	9
Pt2	8a	0.3754(2)	$x$	$x$	0.97(2)	–3Ge3 – 2.508(7)	9
Pt3	24c	0.1233(2)	0.3772(2)	0.3783(2)	0.73(1)	–1Ge6 – 2.538(9)	9
Pt4	24c	0.1243(2)	0.1251(2)	0.3763(2)	1.01(1)	–1Ge6 – 2.475(9)	9
Ge1 <sup>a</sup>	8a	0.2481(2)	$x$	$x$	1.01(2)	–3Ge7 – 2.58(1)	12
Ge2	24c	0.0053(3)	0.3272(3)	0.5775(2)	1.66(2)	–1Pt1 – 2.474(6)	10
Ge3	24c	0.1056(3)	0.2471(4)	0.1813(2)	1.64(2)	–1Ge7 – 2.408(7)	12
Ge4 <sup>b</sup>	24c	0.0039(3)	0.1757(3)	0.4200(4)	0.92(2)	–1Pt4 – 2.486(6)	10
Ge5	24c	0.2478(3)	0.3112(3)	0.3812(4)	1.54(2)	–1Pt3 – 2.545(7)	13
Ge6	24c	0.0612(2)	0.4972(2)	0.1335(5)	1.64(2)	–1Pt4 – 2.475(9)	11
Ge7	24c	0.1213(3)	0.2508(3)	0.3136(4)	1.41(2)	–1Ge3 – 2.408(7)	13
Ge8	24c	0.0044(3)	0.3304(3)	0.0766(4)	1.49(2)	–1Pt4 – 2.486(7)	11
Ge9	24c	0.1740(4)	0.4189(2)	0.2523(3)	1.55(2)	–1Pt3 – 2.565(7)	13
Tl <sup>c</sup>	8a	0.0021(3)	$x$	$x$	1.37(2)	–3Ge6 – 2.632(6)	11
$\text{Yb}_3\text{Pt}_4\text{Ge}_{13}$							
Yb1	2a	0	0	0.0 <sup>d</sup>	0.58(5)	–2Ge3 – 3.209(5)	16
Yb2	2b	1/2	1/2	0.0008(7)	0.72(5)	–4Ge7 – 2.971(7)	16
Yb3	8e	0.1275(1)	0.3780(1)	0.2578(5)	0.75(2)	–1Ge8 – 2.992(4)	16
Pt1	8e	0.2504(1)	0.50110(2)	0.00591(6)	0.40(2)	–1Ge5 – 2.519(4)	9
Pt2	8e	0.0015(2)	0.2519(1)	0.0042(6)	0.44(1)	–1Ge9 – 2.487(8)	9
Ge1	4d	0.1718(4)	$x$	0.1035(8)	0.4(1)	–2Pt2 – 2.560(6)	10
Ge2	4d	0.2471(2)	$x$	0.7577(9)	0.63(3)	–1Ge5 – 2.499(9)	10
Ge3	4d	0.1727(4)	$x$	0.4131(7)	0.8(1)	–2Pt2 – 2.574(6)	12
Ge4	4d	0.3140(3)	$x$	0.0364(7)	1.1(1)	–2Pt1 – 2.535(4)	13
Ge5	4d	0.3108(3)	$x$	0.5111(1)	0.7(1)	–1Ge2 – 2.499(9)	13
Ge6	8e	0.1207(3)	0.6172(3)	0.3693(6)	0.91(5)	–1Pt1 – 2.555(5)	13
Ge7	8e	0.3443(2)	0.4987(2)	0.2553(8)	0.72(4)	–1Pt1 – 2.544(8)	13
Ge8	8e	0.0756(3)	0.5747(3)	0.0925(5)	0.68(5)	–1Pt1 – 2.541(4)	12
Ge9	8e	0.0422(2)	0.1763(2)	0.7512(8)	1.04(5)	–1Ge9 – 2.416(4)	13

<sup>a</sup> Occupancy  $G = 0.62(1)$ . <sup>b</sup> Occupancy  $G = 0.89(1)$ . <sup>c</sup>  $Tl = 6.48(1)$  Ge +  $1.52(1)$  Pt. <sup>d</sup> Fixed for refinement.

tetragonal distortion of the lattice (Fig. 2). 122 peaks of the HR XRD pattern of  $\text{Yb}_3\text{Pt}_4\text{Ge}_{13}$  were successfully indexed on the basis of a tetragonal primitive lattice with unit cell parameters  $a = 12.7479(1)$  Å,  $c = 9.0009(1)$  Å. The observed splitting pattern (e.g.  $h00$ ) reflections split into two with intensity ratio 2 : 1, Fig. 2) as well as the characteristic ratio of the tetragonal lattice parameters ( $a_{\text{tet}} \approx a_{\text{cub}} \sqrt{2}$ ,  $c_{\text{tet}} \approx a_{\text{cub}}$ ; Table 1) corroborates a close relationship of the atomic arrangement to the cubic prototype.

An analysis of the reflection conditions ( $l = 2n$  for  $(0kl)$ ;  $l = 2n$  for  $(00l)$ ) in the HR XRD pattern of  $\text{Yb}_3\text{Pt}_4\text{Ge}_{13}$  indicated 3 possible space groups:  $P4_2/mcm$ ,  $P4_2mc$  and  $P4_2c$  (Fig. 3). The structural model in the space group  $P4_2/mcm$  was obtained using direct methods. The final values of the reliability factors for the corresponding refinement were  $R_1 = 0.077$ ,  $R_p = 0.141$ . However, large displacement parameters for Ge atoms in the general position  $16p$  ( $B_{\text{iso}} = 4.13(2)$  Å<sup>2</sup>) as well as some shortened (by 9%) Ge–Ge contacts suggested the non-centrosymmetric space group  $P4_2mc$ . Details of the refinement, final values of the atomic coordinates and displacement parameters together with the shortest interatomic distances are presented in Tables 1 and 2, respectively. The experimental and calculated powder XRD patterns for  $\text{Yb}_3\text{Pt}_4\text{Ge}_{13}$  are shown in Fig. 3. In the refined structural model, atomic distances mostly agree well with the sum of atomic radii of the elements (Table 2). The refined

displacement parameters indicate a fully ordered occupation of the position. All these facts, as well as the low final values of the  $R$  factors (Table 1) confirm the reliability of the obtained model.

### Crystal chemistry

The crystal structures of  $\text{Pr}_3\text{Rh}_4\text{Sn}_{13}$ <sup>8</sup> and filled skutterudite ( $\text{LaFe}_4\text{P}_{12}$  type<sup>25</sup>) are commonly considered as derivatives of the cubic perovskite structure (space group  $Pm\bar{3}m$ , Fig. 4). The  $\text{CaTiO}_3$  type ( $ABX_3$ )<sup>26</sup> is usually presented as an array of corner-sharing octahedra  $BX_6$ . Cubooctahedral cavities in the free space between octahedra are filled by Ca atoms. One unit cell contains one cubooctahedron  $AX_{12}$  and one octahedron  $BX_6$  (Fig. 4, left). Doubling of the unit cell parameters yields eight cubooctahedra and eight octahedra in the new cell. Tilting of the octahedra, in a way that two of the eight initial cubooctahedra are converted into icosahedra (colored yellow in Fig. 4) and distortion of the second type (red in Fig. 4, middle), leads to the formation of filled skutterudite type  $\text{LaFe}_4\text{P}_{12}$  (space group  $Im\bar{3}$ ). Three of the six distorted cubooctahedra may be considered as two bicapped trigonal prisms sharing a quadratic face (red in Fig. 4, middle). The remaining three can be represented by two tetragonal antiprisms with common quadratic face (blue in Fig. 4). The centers of these polyhedra are empty so that the transformations can be



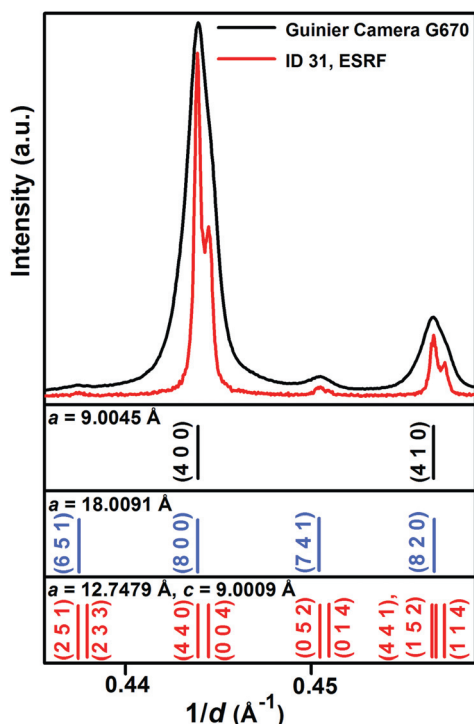


**Fig. 2** Indexing of the powder XRD patterns of  $\text{Yb}_3\text{Pt}_4\text{Ge}_{13}$  (black – laboratory data, HUBER G670 imaging plate Guinier camera ( $\text{CuK}\alpha_1$ ); red – synchrotron data, ESRF ID31,  $\lambda = 0.39987 \text{ \AA}$ ) with cubic primitive ( $a_{\text{cub}} = 9.0045 \text{ \AA}$ ), cubic body-centered ( $a_{\text{doubled}} \approx 2a_{\text{cub}} = 18.0091 \text{ \AA}$ ) and tetragonal lattices ( $a_{\text{tet}} \approx a_{\text{cub}} \sqrt{2}$  and  $c_{\text{tet}} \approx a_{\text{cub}}$ ). In the high-resolution XRD pattern clear splitting of the reflections is observed.

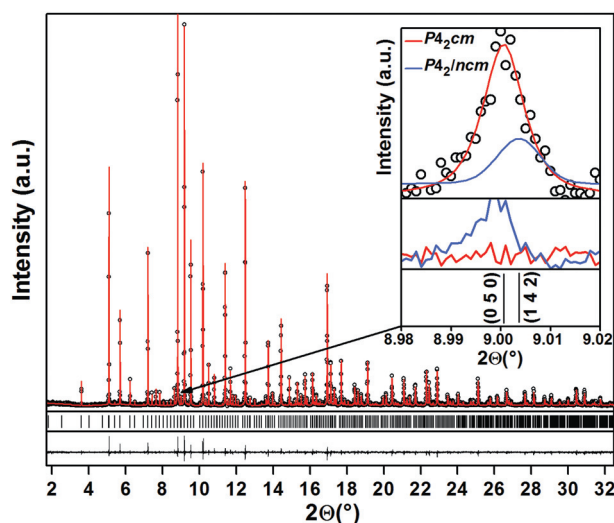


**Fig. 3** Experimental (black points) and calculated (red line) XRD synchrotron patterns ( $\lambda = 0.39987 \text{ (Å)}$ ) of  $\text{Yb}_3\text{Pt}_4\text{Ge}_{13}$ . Peak positions are given by black ticks; the difference plot is shown as a black line in the bottom part. Inset:  $2\theta$  range of  $8.98\text{--}9.02^\circ$  for the models in the space groups  $P4_2cm$  and  $P4_2/nm$ . Reflection  $(0\ 5\ 0)$ , which breaks the reflection condition  $h + k = 2n$  for  $(hk0)$ , confirms the true choice of the non-centrosymmetric space group.

balanced as follows:

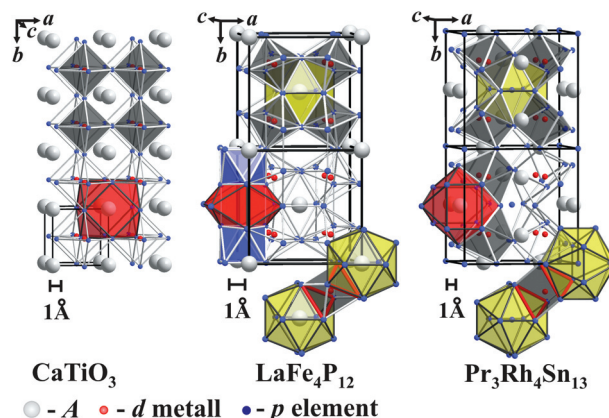
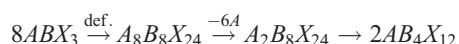
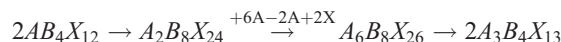


**Fig. 4** Relationship between the crystal structures of  $\text{CaTiO}_3$ ,  $\text{Pr}_3\text{Rh}_4\text{Sn}_{13}$  and  $\text{LaFe}_4\text{P}_{12}$  types (see text).

Rotation of the icosahedron located at the body center of the cell in the  $\text{LaFe}_4\text{P}_{12}$  type by  $90^\circ$  around an axis parallel to a cube edge leads to a transformation of the octahedron around the  $B$  atom into a trigonal prism (gray in Fig. 4, right). This geometrical rearrangement is indicated in Fig. 4 right, where respective triangular faces of the trigonal prism and octahedron (trigonal antiprism) are marked by thick red lines. The appearance of an array of corner-sharing trigonal prisms in the new structure is accompanied by a change of the symmetry to  $Pm\bar{3}n$ .<sup>27</sup> Less distorted cubooctahedra (red in Fig. 4, right), as compared to the  $\text{LaFe}_4\text{P}_{12}$  type, are filled by Pr (similar as in the perovskite structure). The icosahedra are filled by additional  $X$  atoms (yellow in Fig. 4, right), as this was already found in the skutterudite  $\text{Sn}_x\text{Pt}_4\text{Sn}_y\text{Sb}_{12-y}$ .<sup>28</sup> The so-formed structure is known as the  $\text{Pr}_3\text{Rh}_4\text{Sn}_{13}$  type.<sup>8</sup> The composition transformation may be described by the following equation:



Both structures,  $\text{Ca}_3\text{Pt}_{4+x}\text{Ge}_{13-y}$  and  $\text{Yb}_3\text{Rh}_4\text{Sn}_{13}$ , as well as  $\text{La}_3\text{Rh}_4\text{Sn}_{13}$ <sup>21</sup> show the same structural motif as in the  $\text{Pr}_3\text{Rh}_4\text{Sn}_{13}$  prototype (Fig. 5). The only difference is, that in  $\text{Pr}_3\text{Rh}_4\text{Sn}_{13}$  icosahedra and trigonal prisms are regular while in all three derivative structures they are distorted. However, it should be noted that interatomic distances are very different in all these compounds, especially in the  $X$ -atom networks.

Most interatomic distances in the structure of  $\text{Pr}_3\text{Rh}_4\text{Sn}_{13}$ <sup>8,23</sup> are slightly larger than the sums of atomic radii of elements ( $r_{\text{Pr}} = 1.83 \text{ \AA}$ ,  $r_{\text{Rh}} = 1.34 \text{ \AA}$ ,  $r_{\text{Sn}} = 1.41 \text{ \AA}$ ).<sup>29</sup> Only the Rh–Sn contacts are shortened by  $\sim 3\%$ . If one assumes bonding limits within the sum of atomic radii ( $d_{\text{min}}$ ) multiplied by  $\sqrt{2}$ ,<sup>30</sup> then the coordination number (CN) for the Pr atom in this structure is 16 and the coordination polyhedron (CP) is a distorted cubooctahedron with 4 additional vertices. For the Rh atoms we have CN = 9 (three-capped trigonal prism), for Sn1 CN = 12 (regular icosahedron), and for Sn2 CN = 14 (14-vertices polyhedron). In the planar nets occurring at  $y = 1/2$  the Sn-atoms form chains of condensed triangles and rectangles (Fig. 5, left panel). In the structure of  $\text{La}_3\text{Rh}_4\text{Sn}_{13}$ <sup>21</sup> the Rh–Sn contacts are shortened already by  $\sim 4\%$ , however, other distances are still larger than the sums of atomic radii of elements ( $r_{\text{La}} = 1.88 \text{ \AA}$ ).<sup>29</sup> Some Sn–Sn

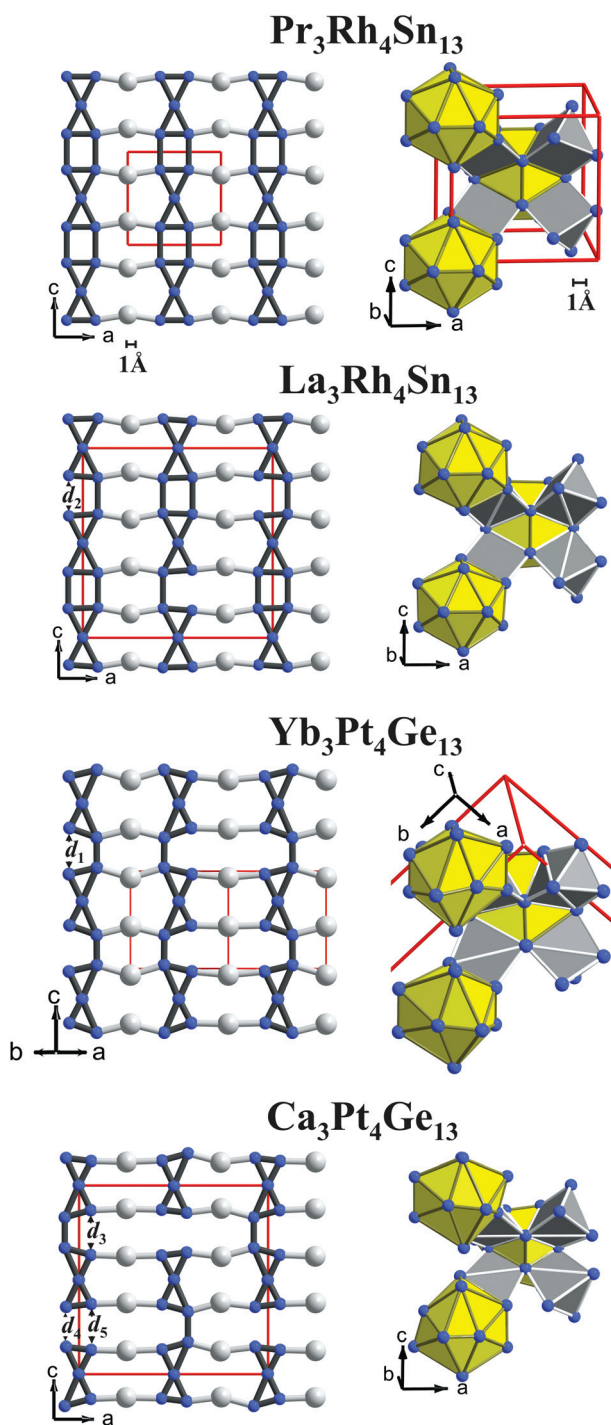


**Fig. 5**  $\text{Pr}_3\text{Rh}_4\text{Sn}_{13}$  prototype and related structures: (left panel) planar nets occurring at  $y = 1/2$  with interatomic contacts which do not exceed the distance limit  $d_{\min} \sqrt{2}$ ,  $2.978(1) \text{ \AA} \leq d \leq 3.738(2) \text{ \AA}$  for  $\text{Pr}_3\text{Rh}_4\text{Sn}_{13}$ ;  $2.499(9) \text{ \AA} \leq d \leq 3.40(1) \text{ \AA}$ ,  $d_1 = 4.273(9) \text{ \AA}$  for  $\text{Yb}_3\text{Pt}_4\text{Ge}_{13}$ ;  $2.98(2) \text{ \AA} \leq d \leq 3.77(1) \text{ \AA}$ ,  $d_2 = 4.16(1) \text{ \AA}$  for  $\text{La}_3\text{Rh}_4\text{Sn}_{13}$  and  $2.407(7) \text{ \AA} \leq d \leq 3.36(1) \text{ \AA}$ ,  $d_3 = 4.291(8) \text{ \AA}$ ,  $d_4 = 3.82(1) \text{ \AA}$ ,  $d_5 = 4.38(1) \text{ \AA}$  for  $\text{Ca}_3\text{Pt}_{4+x}\text{Ge}_{13-y}$ ; (right panel) regular icosahedra ( $\text{Pr}_3\text{Rh}_4\text{Sn}_{13}$ ) or distorted icosahedra ( $\text{La}_3\text{Rh}_4\text{Sn}_{13}$ ,  $\text{Ca}_3\text{Pt}_{4+x}\text{Ge}_{13-y}$  and  $\text{Yb}_3\text{Pt}_4\text{Ge}_{13}$ ) interlinked by corner-sharing distorted trigonal prisms.

contacts exceed the  $d_{\min} \sqrt{2}$  limit, leading to the distortions in the nets analogous to those observed in  $\text{Pr}_3\text{Rh}_4\text{Sn}_{13}$  (Fig. 5, left panel).

The situation concerning the interatomic distances changes significantly when going to the germanides  $\text{Ca}_3\text{Pt}_{4+x}\text{Ge}_{13-y}$  and  $\text{Yb}_3\text{Pt}_4\text{Ge}_{13}$  ( $r_{\text{Ca}} = 1.97 \text{ \AA}$ ,  $r_{\text{Yb}} = 1.94 \text{ \AA}$ ,  $r_{\text{Pt}} = 1.38 \text{ \AA}$ ,  $r_{\text{Ge}} = 1.23 \text{ \AA}$ ).<sup>29</sup>  $A$ -Pt contacts become shorter by 6% and 4.2% respectively (Table 2);  $A$ -Ge distances shrink by 6% and even by 8.7% in the case of  $\text{Ca}_3\text{Pt}_{4+x}\text{Ge}_{13-y}$ . Similar as the Rh-Sn contacts in the  $\text{Pr}_3\text{Rh}_4\text{Sn}_{13}$  and  $\text{La}_3\text{Rh}_4\text{Sn}_{13}$  stannides, the Pt-Ge distances in the structures of  $\text{Ca}_3\text{Pt}_{4+x}\text{Ge}_{13-y}$  and  $\text{Yb}_3\text{Pt}_4\text{Ge}_{13}$  germanides are shortened by 5.2% and 4.7%. Ge-Ge contacts are close to the sum of atomic radii (shortening by only  $\sim 2\%$  in both compounds, Table 2). A characteristic feature of all the compounds is the absence of short  $T$ - $T$  contacts.

The shortening of  $A$ -Pt and  $A$ -Ge distances in the structures of  $\text{Ca}_3\text{Pt}_{4+x}\text{Ge}_{13-y}$  and  $\text{Yb}_3\text{Pt}_4\text{Ge}_{13}$  is also accompanied by the increase of some Ge-Ge distances, which leads to the reduction of the CN of Ge atoms. In the crystal structure of the  $\text{Pr}_3\text{Rh}_4\text{Sn}_{13}$  prototype Sn atoms adopt CN = 12 (icosahedron) and 14 (14-vertices polyhedron). In the new germanides, the CN for Ge atoms vary between 10 and 13 (Fig. 5, left panel). In the net at  $y = 1/2$ , analogous to those in the structure of  $\text{Pr}_3\text{Rh}_4\text{Sn}_{13}$  type, more Ge-Ge contacts are broken (Fig. 5, left panel).

The atoms  $A = \text{Ca}$ ,  $\text{La}$ ,  $\text{Yb}$  and  $T = \text{Rh}$ ,  $\text{Pt}$  in the stannide and germanide derivatives remain almost in the same positions as in the prototype, while distortions in the  $X = \text{Ge}$ ,  $\text{Sn}$  sublattices lead to the loss of the center of symmetry (for  $\text{La}_3\text{Rh}_4\text{Sn}_{13}$  and  $\text{Ca}_3\text{Pt}_{4+x}\text{Ge}_{13-y}$ ) or even to a further reduction of symmetry, as observed for  $\text{Yb}_3\text{Pt}_4\text{Ge}_{13}$ .

Such close and subtle relationship between these 4 structure types explains the close resemblance of the observed XRD powder patterns on a low level of resolution.

### Electronic structures

The crystal structures of  $\text{Ca}_3\text{Pt}_{4+x}\text{Ge}_{13-y}$  and  $\text{Yb}_3\text{Pt}_4\text{Ge}_{13}$  are rather complex. To facilitate a qualitative interpretation of the electronic structures, we first present the results for the ideal cubic  $\text{Ca}_3\text{Pt}_4\text{Ge}_{13}$  in the undistorted structure of the  $\text{Pr}_3\text{Rh}_4\text{Sn}_{13}$  type, where the lattice parameter is set to  $a = 9.0289 \text{ \AA}$  and atomic positions relaxed to find the equilibrium structure. The resulting electronic density of states (DOS) (Fig. 6) features Ge 4s and Pt 6s states lying between  $-13$  and  $-7 \text{ eV}$ . The broad valence band above  $-6 \text{ eV}$  is formed by Ge 4p states, with a large contribution of Pt 5d states below  $E_F$  and Ca 4s states above the Fermi level. The electronic DOS for the idealized cubic structure of  $\text{Ca}_3\text{Pt}_4\text{Ge}_{13}$  suggests a predominantly ionic bonding between  $\text{Ca}^{2+}$  and the Pt-Ge anionic framework.

Pt retains the 5d shell nearly filled (8.75 out of 10 electrons below the Fermi level). This shifts Pt states to lower energies. The Pt d-states are split into two groups: one at  $-6 \text{ eV} < E < -4 \text{ eV}$  reflects more localized states; the other—below  $-8 \text{ eV}$  and above  $-4 \text{ eV}$ —represents electrons participating in the bonding with Ge. This indicates covalent Pt-Ge interactions, which are well in agreement with the close electronegativities of both elements. The itinerant states at the Fermi level mostly originate from Ge 4p. The idealized crystal structure features two Ge positions, with Ge1 forming the Pt-Ge framework and Ge2 occupying the icosahedral voids. Both types of Ge atoms produce similar contributions to the bands at the Fermi level which is

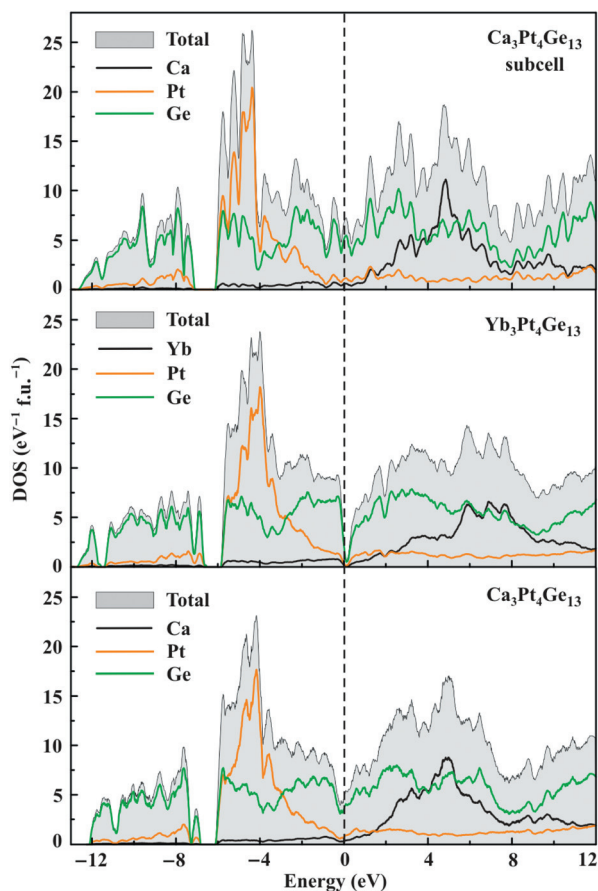


**Fig. 6** (top panel) Calculated electronic density of states (DOS) for the idealized cubic structure (subcell) of  $\text{Ca}_3\text{Pt}_4\text{Ge}_{13}$  (top panel), experimental crystal structures of  $\text{Yb}_3\text{Pt}_4\text{Ge}_{13}$  (middle panel) and  $\text{Ca}_3\text{Pt}_{4+x}\text{Ge}_{13-y}$  (bottom panel). The Fermi level is indicated by the dashed line. The 4f orbitals of Yb were considered as core states and, therefore, are not present in the figure. For the Ca compound, the stoichiometric composition and the fully ordered crystal structure were assumed (see text).

located on a spike of the DOS, suggesting the instability of the idealized cubic structure.

The electronic structures of  $\text{Yb}_3\text{Pt}_4\text{Ge}_{13}$  and stoichiometric  $\text{Ca}_3\text{Pt}_4\text{Ge}_{13}$  in the experimentally observed supercells show both the ionic state of  $\text{Ca}^{2+}$  and  $\text{Yb}^{2+}$ , the large filling of the Pt 5d shell, and the predominantly Ge 4p states at the Fermi level (Fig. 7). However, the Fermi level is now located in a dip of the DOS, which is especially well pronounced in the Yb compound.

Since the dip around 0 eV is missing in the idealized cubic structure of  $\text{Ca}_3\text{Pt}_4\text{Ge}_{13}$  (Fig. 6), the emergence of this dip is attributed to the slight structural reorganization and the formation of superstructures. A closer inspection of the idealized cubic structure and real crystal structures established in this work reveals a change in the arrangement of Ge atoms. The idealized structure features Ge1 atoms forming the Pt–Ge framework and Ge2 atoms located in the voids. The Ge1–Ge2 distances exceed 3 Å and indicate a rather weak bonding for the Ge2 site. The superstructures reveal shortened Ge1–Ge2 distances that evidence the formation of covalent bonds and the involvement of all Ge atoms into the anionic framework. The formation of additional Ge–Ge bonds naturally leads to the separation of Ge

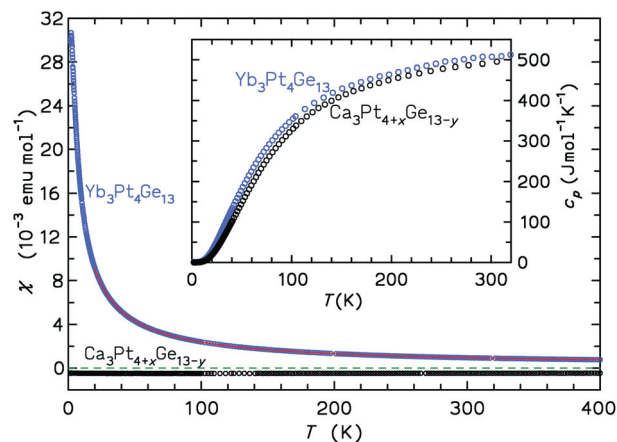


**Fig. 7** Molar magnetic susceptibilities,  $\chi(T)$ , of  $\text{Ca}_3\text{Pt}_{4+x}\text{Ge}_{13-y}$  (black circles) and  $\text{Yb}_3\text{Pt}_4\text{Ge}_{13}$  (blue circles). The modified Curie–Weiss fit (see text) for the Yb compound is indicated by a red line. Zero susceptibility is indicated by dashed green line, as guide for eyes only. The inset shows the molar heat capacities. In the case of  $\text{Ca}_3\text{Pt}_{4+x}\text{Ge}_{13-y}$  both molar properties were calculated for  $x = 0$  and  $y = 0$ , i.e. for the idealized composition  $\text{Ca}_3\text{Pt}_4\text{Ge}_{13}$ .

4p states into the bonding and antibonding bands, and to the ensuing reduction of the DOS at the Fermi level. Particularly, we found  $N(E_F) = 2.2 \text{ eV}^{-1}/\text{f.u.}$  and  $3.3 \text{ eV}^{-1}/\text{f.u.}$  in  $\text{Yb}_3\text{Pt}_4\text{Ge}_{13}$  and stoichiometric  $\text{Ca}_3\text{Pt}_4\text{Ge}_{13}$ , respectively. Replacing Ge2 by Pt in the Ca compound will likely lead to a further reduction in the DOS at Fermi level, thus supporting the stabilization of the crystal structure.

### Physical properties

The magnetic susceptibilities,  $\chi(T)$ , of the  $\text{Ca}_3\text{Pt}_{4+x}\text{Ge}_{13-y}$  and  $\text{Yb}_3\text{Pt}_4\text{Ge}_{13}$  species, for the latter together with a fit to a modified Curie–Weiss law in the temperature range 20–400 K, are shown in Fig. 7. The obtained fitting parameters are  $\chi_0 = +2.0 \times 10^{-4} \text{ emu mol}^{-1}$ ,  $C = 0.230 \text{ emu mol}^{-1} \text{ K}$  and  $\theta_p = -6.0 \text{ K}$ , suggesting antiferromagnetic interactions. For the  $\text{Yb}_3\text{Pt}_4\text{Ge}_{13}$  sample a cusp at  $T_N = 2.3 \text{ K}$  in  $\chi(T)$  is observed in low fields ( $\mu_0 H \leq 0.1 \text{ T}$ ). It is attributed to antiferromagnetic ordering of the  $\text{Yb}^{3+}$  moments in the impurity phase  $\text{Yb}_2\text{O}_3$ .<sup>31</sup> Assigning the whole paramagnetic moment of the  $\text{Yb}_3\text{Pt}_4\text{Ge}_{13}$  sample to the  $\text{Yb}_2\text{O}_3$  impurity, the effective magnetic moment  $\mu_{\text{eff}}$  of  $1.36 \mu_B$  per formula unit (derived from  $C$ ) corresponds to 9.0%  $\text{Yb}^{3+}$  species and thus 0.8 wt% of  $\text{Yb}_2\text{O}_3$  in the sample. This finding is in fair agreement with the results from XAS, RIXS and EDXS studies reported below. No signature of  $\text{Yb}_2\text{O}_3$  is observed in the XRD data, since 0.8 wt% is below the estimation limit of the method.

The susceptibility of  $\text{Ca}_3\text{Pt}_{4+x}\text{Ge}_{13-y}$  is negative with a weak positive linear temperature dependence caused by minor paramagnetic impurities (assuming magnetic species or charged point defects with a  $S = 1/2$  moment the concentration is 0.10 mol%). The extrapolated  $\chi_0$  at  $T = 0 \text{ K}$  is  $-505 \times 10^{-6} \text{ emu mol}^{-1}$ . No superconductivity or other phase transitions were observed for both compounds down to 1.8 K in fields  $\mu_0 H \geq 2 \text{ mT}$ .



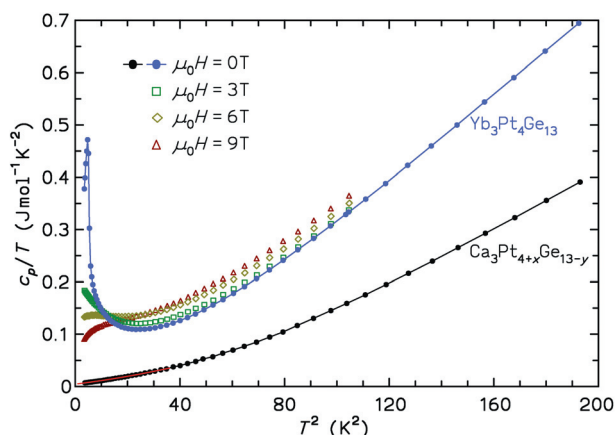


**Fig. 8** Low-temperature specific heat  $c_p(T, H)$  for  $\text{Ca}_3\text{Pt}_{4+x}\text{Ge}_{13-y}$  (black circles with line) and  $\text{Yb}_3\text{Pt}_4\text{Ge}_{13}$  (blue circles with line as guide for eye only) in zero field. For the Yb compound also data for different magnetic fields are shown. The fit (see text) to the  $\text{Ca}_3\text{Pt}_{4+x}\text{Ge}_{13-y}$  data for  $T^2 < 36 \text{ K}^2$  is indicated by a red line.

The molar heat capacities  $c_p(T)$  of both samples are given in the inset of Fig. 7. The values of  $492 \text{ J mol}^{-1} \text{ K}^{-1}$  and  $507 \text{ J mol}^{-1} \text{ K}^{-1}$  observed at 298 K for the Ca and Yb compound agree well with the Dulong–Petit law ( $c_p \approx 3nR$ , where  $n$  is the number of atoms per f.u.). Generally, the specific heat of  $\text{Yb}_3\text{Pt}_4\text{Ge}_{13}$  is slightly larger than for  $\text{Ca}_3\text{Pt}_{4+x}\text{Ge}_{13-y}$  since the heavier Yb atoms (compared to Ca) lead to a lower Debye temperature. The low-temperature specific heats are given in Fig. 8 in a  $c_p/T$  vs.  $T^2$  representation. The Ca compound data for  $T < 6 \text{ K}$  can be described by  $c_p(T) = \gamma T + \beta T^3 + \delta T^5$ , where  $\gamma$  is the Sommerfeld coefficient of the electronic heat capacity, and  $\beta$  and  $\delta$  are the first terms of the harmonic lattice approximation for the phonon contribution. The positive deviation of  $c_p(T)$  at higher temperatures is due to Einstein-like phonon modes which arise from vibration of the weakly bonded Ca atoms in their large atomic cages. No sensible model including these Einstein modes in order to describe  $c_p(T)$  at higher temperatures, as for  $\text{MFe}_4\text{Sb}_{12}$ <sup>32</sup> or  $\text{MPt}_4\text{Ge}_{12}$ <sup>9</sup> filled skutterudite compounds, could be found for  $\text{Ca}_3\text{Pt}_{4+x}\text{Ge}_{13-y}$ . A fit with the simple relation above (see red line in Fig. 9), in a temperature range of 1.8–6 K results in  $\gamma = 4.4 \text{ mJ mol}^{-1} \text{ K}^{-2}$ ,  $\beta = 6.2 \times 10^{-4} \text{ J mol}^{-1} \text{ K}^{-4}$  corresponding to an initial Debye temperature  $\theta_D(0) = 398 \text{ K}$ , and  $\delta = 6.6 \times 10^{-6} \text{ J mol}^{-1} \text{ K}^{-6}$ . The small value of  $\gamma$  indicates a low DOS at the Fermi level of  $\approx 1.9 \text{ states eV}^{-1} \text{ f.u.}^{-1}$  and metallic properties of  $\text{Ca}_3\text{Pt}_{4+x}\text{Ge}_{13-y}$ .

The specific heat of the  $\text{Yb}_3\text{Pt}_4\text{Ge}_{13}$  sample below 6 K is dominated by the antiferromagnetic ordering transition of the  $\text{Yb}_2\text{O}_3$  impurity, which is smeared out to higher temperatures with increasing external magnetic field (see Fig. 8). The tentative fit to the equation given above leads to the values of the Debye temperature ( $\theta_D(0) \sim 310 \text{ K}$ , lower than for  $\text{Ca}_3\text{Pt}_{4+x}\text{Ge}_{13-y}$ ) and the electronic coefficient  $\gamma$  ( $< 50 \text{ mJ mol}^{-1} \text{ K}^{-2}$ ). However, these values are estimated with relatively low precision, because we have to account for the  $\text{Yb}_2\text{O}_3$  contribution using an additional  $a/T^2$  term that approximates the high temperature limit of the magnetic specific heat. Nevertheless, our tentative estimate consistently shows the low coefficient  $\gamma$ , which would not support

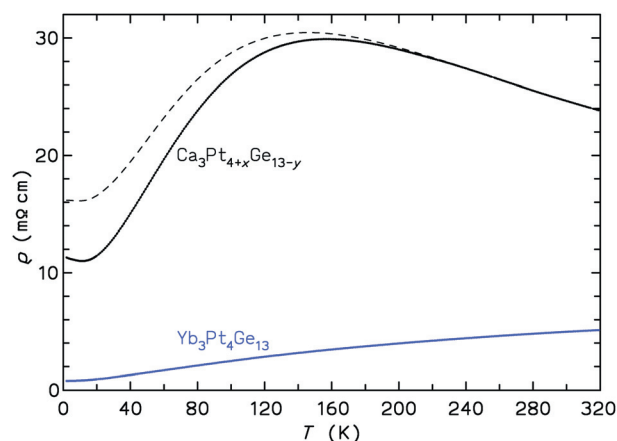


**Fig. 9** Electrical resistivity  $\rho(T)$  of polycrystalline  $\text{Yb}_3\text{Pt}_4\text{Ge}_{13}$  (full blue line) and of polycrystalline  $\text{Ca}_3\text{Pt}_{4+x}\text{Ge}_{13-y}$  in zero magnetic field (full black line) and in a field  $\mu_0 H = 9 \text{ T}$  (dashed black line).

an intermediate valence state, thus confirming the divalent state of Yb species in  $\text{Yb}_3\text{Pt}_4\text{Ge}_{13}$ .

The electrical resistivities,  $\rho(T)$ , of the polycrystalline pieces of both compounds are displayed in Fig. 9. The residual resistance ratio of 6.3 indicates a reasonably good crystalline quality with respect to disorder and defects. Albeit having a temperature dependence typical for a metal, both the residual ( $\rho_0 = 0.8 \text{ m}\Omega \text{ cm}$ ) as well as the room-temperature resistivity ( $\rho(300 \text{ K}) = 5.0 \text{ m}\Omega \text{ cm}$ ) of  $\text{Yb}_3\text{Pt}_4\text{Ge}_{13}$  are very high and well above the Ioffe–Regel limit ( $\sim 0.1 \text{ m}\Omega \text{ cm}$ ). The magnetoresistance increase is largest for the minimum temperature (1.8 K) and amounts to +9.3%.

The  $\text{Ca}_3\text{Pt}_{4+x}\text{Ge}_{13-y}$  sample shows even higher resistivity: the residual resistivity is  $\rho_0 = 11.3 \text{ m}\Omega \text{ cm}$ , then, with increasing temperature,  $\rho(T)$  goes through a shallow minimum of  $\rho_{\min} = 11.0 \text{ m}\Omega \text{ cm}$  at 11.0 K, then shows an increase and a maximum of  $\rho_{\min} = 30.0 \text{ m}\Omega \text{ cm}$  at 157 K, and finally decreases again ( $\rho(300 \text{ K}) = 23.8 \text{ m}\Omega \text{ cm}$ ). Such values and temperature characteristics can be found in doped (impure) semiconductors. This finding suggests that the off-stoichiometric composition of  $\text{Ca}_3\text{Pt}_{4+x}\text{Ge}_{13-y}$  leads to the impurities that capture charge carriers, or triggers the formation of a small band gap. This would be in agreement with a much smaller DOS at  $E_F$  derived from the electronic specific heat coefficient  $\gamma$  ( $1.9 \text{ eV}^{-1} \text{ f.u.}^{-1}$ ) rather than from the electronic structure calculation ( $3.3 \text{ eV}^{-1} \text{ f.u.}^{-1}$ ). The magnetoresistance increase for  $\text{Ca}_3\text{Pt}_{4+x}\text{Ge}_{13-y}$  is the largest at  $T \approx 13 \text{ K}$  and amounts to 47%, in agreement with a very low concentration of mobile charge carriers. The magnetoresistance decreases gradually with increasing temperature and vanishes above the temperature of the resistivity maximum.

**Spectroscopic study of  $\text{Yb}_3\text{Pt}_4\text{Ge}_{13}$ .** X-Ray absorption spectra measured at the Yb  $L_{\text{III}}$  edge (Fig. 10) at  $T = 5 \text{ K}$  and  $293 \text{ K}$  are coincident. They show one dominant maximum reflecting the contribution of Yb with  $4f^{14}$  configuration ( $\text{Yb}^{2+}$ ). Additionally, both spectra reveal a shoulder on the higher energy side that indicates contributions of the  $4f^{13}$  ( $\text{Yb}^{3+}$ ) state. This can be explained by the presence of the  $\text{Yb}_2\text{O}_3$  impurity in the sample, as further evidenced by  $\chi(T)$ ,  $c_p(T)$  and WDXS studies.

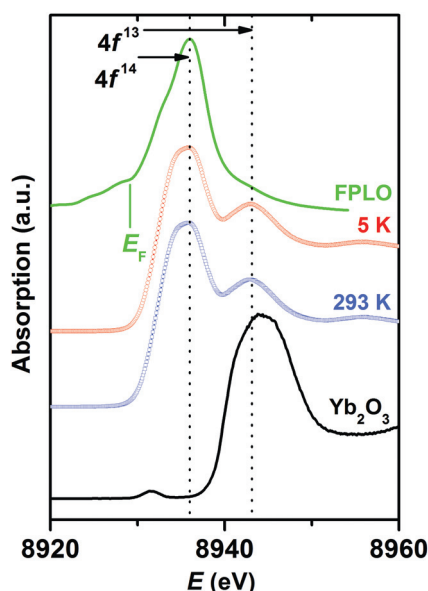


**Fig. 10** Experimentally obtained high energy resolution XANES (HERFD) at the Yb  $L_{III}$  edge of  $\text{Yb}_3\text{Pt}_4\text{Ge}_{13}$  and  $\text{Yb}_2\text{O}_3$  together with the theoretically (FPLO) calculated Yb 5d DOS of  $\text{Yb}_3\text{Pt}_4\text{Ge}_{13}$ .

The contribution of Yb 5d electrons to the DOS, obtained from the *ab initio* electronic structure calculations using the FPLO code, is shown in Fig. 10. The indicated Fermi level  $E_F$  separates the occupied and unoccupied states. The calculated DOS curve was shifted to coincide with the maximum of the main edge absorption transition of  $\text{Yb}_3\text{Pt}_4\text{Ge}_{13}$ . It describes well the first absorption maximum and confirms also a negligible contribution of  $\text{Yb}^{2+}$  with  $4f^{14}$  configuration to the maximum at higher energy, which is a clear indication of the presence of  $\text{Yb}^{3+}$  species with  $4f^{13}$  configuration ( $\text{Yb}_2\text{O}_3$ ) in the measured XANES spectra of the  $\text{Yb}_3\text{Pt}_4\text{Ge}_{13}$  sample.

Fig. 11 shows the experimental (left) and theoretical (right) core-to-valence resonant inelastic X-ray scattering (RIXS)<sup>33</sup> profiles of the  $\text{Yb}_3\text{Pt}_4\text{Ge}_{13}$  and  $\text{Yb}_2\text{O}_3$  compounds. The RIXS data are shown here as a contour map in a plane of incident and transferred photon energies, where the vertical axis represents the energy difference between the incident and emitted energies. The experimental data were obtained with excitation energies near the maximum of the main Yb  $L_{III}$  absorption edge. Two types of excitations are observed: elastic scattering at  $\sim 0$  eV and inelastic scattering features at higher energy transfer. Core-to-valence RIXS calculations at the Yb  $L_{III}$  edge were performed by inserting the Yb 5d pDOS into the Kramers–Heisenberg equation:<sup>34</sup>

$$F(\Omega, \omega) = \int_{\varepsilon} d\varepsilon \frac{\rho(\varepsilon)\rho'(\varepsilon + \Omega - \omega)}{(\varepsilon - \omega)^2 + (\Gamma_n^2/4)} \quad (1)$$

where  $\rho$  and  $\rho'$  are densities of the occupied and unoccupied Yb 5d states, respectively, while  $\Omega$  and  $\omega$  represent the energies of the incident and scattered photons, respectively;  $\Gamma_n$  is the lifetime broadening of the Yb  $2p_{3/2}$  state, which is of 4.6 eV.<sup>35</sup> The validity of this approximation<sup>34</sup> can be evaluated by comparison of experimental and theoretical results.<sup>33</sup> An elastic peak due to

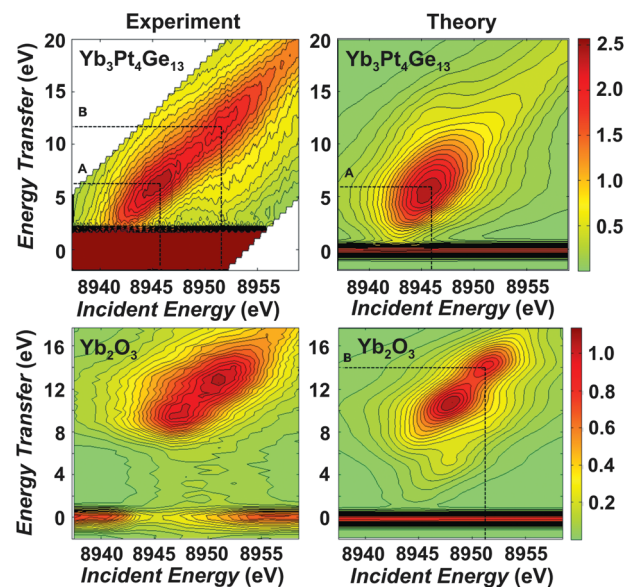


**Fig. 11** Full experimental (left) and theoretical (right) core-to-valence RIXS intensities displayed as contour maps with axes corresponding to incident and transferred energies over the Yb  $L_{III}$  absorption edge of the  $\text{Yb}_3\text{Pt}_4\text{Ge}_{13}$  (top) and  $\text{Yb}_2\text{O}_3$  (bottom) compounds. Variations of the colors in the plot relate to the different scattering intensities.

Thomson scattering was added to the RIXS planes to facilitate comparison with experiment.

The idea to relate the RIXS spectral features to the DOS was initially introduced by Jimenez-Mier *et al.*<sup>34</sup> The RIXS process at the Yb  $L_{III}$  edge is identified as the convolution of the occupied and unoccupied Yb 5d DOS. Here we used the projected DOS obtained in full multiple scattering FEFF 9.0<sup>36</sup> calculations. The input files are based on the crystal structure of  $\text{Yb}_3\text{Pt}_4\text{Ge}_{13}$  (Tables 1 and 2) and the crystal structure of  $\text{Yb}_2\text{O}_3$  reported in the literature.<sup>31</sup> Calculations are made for all the Yb atoms in a cluster of  $\sim 60$  atoms (6.0 Å radius) for both structures. Full multiple scattering (FMS) calculations are performed using a Hedin–Lundqvist self-energy correction and other standard cards. More details about the FEFF code are reported elsewhere.<sup>36</sup>

Experimental RIXS data for  $\text{Yb}_3\text{Pt}_4\text{Ge}_{13}$  (Fig. 11) demonstrate the splitting of the RIXS features in the valence band at  $\sim 6$  and  $\sim 12$  eV in energy transfer (marked A and B) which arise from the two contributions of  $\text{Yb}^{2+}$  and  $\text{Yb}^{3+}$ , respectively, to the XANES spectrum. Feature A can be reproduced by theoretical calculations reported in Fig. 6 with respect to feature shape, position and relative intensities. However, feature B cannot be simulated by this model.

Nevertheless, we find a reasonably good agreement between theoretical calculations and experimental RIXS data for  $\text{Yb}_2\text{O}_3$  (Fig. 11). A detailed examination of the RIXS data for  $\text{Yb}_2\text{O}_3$  reveals that the shape and position of the feature B in the RIXS plane of  $\text{Yb}_3\text{Pt}_4\text{Ge}_{13}$  is similar to the one reported in the RIXS plane for  $\text{Yb}_2\text{O}_3$  (marked feature B in Fig. 11). This is an additional indication that feature B in the RIXS plane of  $\text{Yb}_3\text{Pt}_4\text{Ge}_{13}$  arises from the impurity  $\text{Yb}_2\text{O}_3$  in the  $\text{Yb}_3\text{Pt}_4\text{Ge}_{13}$  sample.



## Conclusions

Applying high-pressure synthesis, new ternary germanides  $\text{Ca}_3\text{Pt}_{4+x}\text{Ge}_{13-y}$  with cubic structure ( $p = 8(1)$  GPa;  $T = 850$  (100) °C for 2 h) and tetragonal  $\text{Yb}_3\text{Pt}_4\text{Ge}_{13}$  ( $p = 2(1)$  GPa;  $T = 800(100)$  °C for 2 hours) were synthesized. Their crystal structures are closely related to the  $\text{Pr}_3\text{Rh}_4\text{Sn}_{13}$  type. Distortions in the Ge sublattice reduce the symmetry of the new structures. X-Ray absorption spectroscopy, resonant inelastic X-ray scattering, magnetic susceptibility and specific heat measurements suggest that the Yb atoms in  $\text{Yb}_3\text{Pt}_4\text{Ge}_{13}$  adopt a temperature-independent  $4f^{14}$  ( $\text{Yb}^{2+}$ ) configuration.  $\text{Ca}_3\text{Pt}_{4+x}\text{Ge}_{13-y}$  is diamagnetic with a very low concentration of mobile charge carriers, which is in agreement with a low density of states at the Fermi level ( $1.9 \text{ eV}^{-1} \text{ f.u.}^{-1}$ ).

## Experimental

### Synthesis

The precursor samples with the molar ratios  $\{\text{Ca}, \text{Yb}\} : \text{Pt} : \text{Ge}$  of 3 : 4 : 13 were prepared by arc melting of the metals Ca (Alfa Aesar, 99.987 wt%), Yb (Ames, 99.9 wt%), Pt (ChemPur, 99.9 wt%) and semiconductor-grade Ge (ChemPur, 99.9999 wt%). The resulting ingots were placed in glassy-carbon crucibles, sealed in tantalum tubes, which were then encapsulated in the evacuated quartz ampoules. After annealing at 700 °C for 7 days the tubes were quenched in water. Sample handling including the prearrangement of the high-pressure setup was performed in argon-filled glove boxes (MBraun,  $p(\text{H}_2\text{O}) < 1 \text{ ppm}$ ;  $p(\text{O}_2) < 1 \text{ ppm}$ ).

High-pressure and high-temperature preparation experiments have been performed in a multi-anvil press. Force redistribution is realized by a Walker module and MgO octahedra with an edge length of 18 mm.<sup>37</sup> Elevated temperatures are realized by resistive graphite heaters. The pressure and temperature calibration is performed in separate calibration experiments by *in situ* monitoring of the resistance changes in bismuth<sup>38,39</sup> and by heating runs with a thermocouple, respectively. Hexagonal boron nitride proved suitable as a crucible material. In order to avoid contamination with oxygen, the high-pressure assembly was transferred to the press directly before synthesis. After the experiment, the setup was immediately removed from the Walker module and transferred back into a glove box, where the sample was recovered from the crucible. However, despite all precautions a small amount of  $\text{Yb}_2\text{O}_3$  (<0.8 wt%) was detected in the studied samples by physical properties and WDXS studies.

To optimize the syntheses, samples with stoichiometric 3 : 4 : 13 compositions were pressed at 2, 4, 6 and 8 GPa and temperatures of 800(100) °C, 850(100) °C and 900(100) °C. In the case of  $\text{Ca}_3\text{Pt}_{4+x}\text{Ge}_{13-y}$  the single phase sample was obtained at 8(1) GPa and a temperature of 850(100) °C. In the samples synthesized under other conditions besides the cubic compound  $\text{CaPtGe}_2$ ,  $\text{PtGe}_2$  and Ge were observed always as additional phases.  $\text{Yb}_3\text{Pt}_4\text{Ge}_{13}$  was synthesized at 2(1) GPa and 800 (100) °C. At higher pressures and temperatures tetragonal  $\text{Yb}_3\text{Pt}_4\text{Ge}_{13}$  decomposes partially, so that also free Ge as well as  $\text{PtGe}_2$  are observed in the XRD powder patterns.

The synthesized products could be separated easily from the crucibles, thus no notable reaction with BN was observed. This was confirmed by powder XRD and energy dispersive X-ray analysis. For the high-pressure syntheses, typical annealing times were 2 h. Samples were allowed to cool down to room temperature before decompression. The resulting samples are dense and stable in air.

**X-Ray diffraction.** All samples were characterized by powder XRD performed on a HUBER G670 imaging plate Guinier camera equipped with a Ge monochromator ( $\text{CuK}_{\alpha 1}$  radiation,  $\lambda = 1.54056 \text{ \AA}$ ). Phase analysis and indexing of diffraction patterns were performed using the WinXPOW program package (STOE WinXPOW, Version 2, STOE and Cie GmbH, Darmstadt). All peaks in the powder diffraction patterns of  $\text{Ca}_3\text{Pt}_{4+x}\text{Ge}_{13-y}$  and  $\text{Yb}_3\text{Pt}_4\text{Ge}_{13}$  compounds could be indexed assuming cubic symmetry and lattice parameter  $a \approx 18 \text{ \AA}$ . However in the case of  $\text{Yb}_3\text{Pt}_4\text{Ge}_{13}$  some reflections were broadened (Fig. 1), which is an indication of a possible symmetry reduction. Therefore, we collected high-resolution powder XRD data with a wavelength of  $0.39987 \text{ \AA}$  at the ID31 beamline of the European Synchrotron Radiation Facility (ESRF). The signal was measured on powder samples contained in thin-walled quartz-glass capillaries with an external diameter of 0.5 mm. Eight scintillation detectors, each preceded by a Si(111) analyzer crystal, in the angle range  $2\theta = 1\text{--}30^\circ$  were used. To achieve good statistics and to avoid the effects of preferred orientation, the capillary was spun during the experiment. Indexing of diffraction patterns, determination of crystal structures as well as full-profile Rietveld refinement were performed using the program package WinCSD.<sup>40</sup>

### Metallography

Polished cuts of the  $\text{Ca}_3\text{Pt}_4\text{Ge}_{13}$  and  $\text{Yb}_3\text{Pt}_4\text{Ge}_{13}$  samples were examined optically (Zeiss Axioplan 2) and by energy-dispersive X-ray spectroscopy (EDXS) on a scanning electron microscope Philips XL30 SEM. The average compositions were  $\text{Ca}_{3.2(2)}\text{Pt}_{3.9(2)}\text{Ge}_{12.9(2)}$  and  $\text{Yb}_{3.1(2)}\text{Pt}_{4.1(2)}\text{Ge}_{12.8(2)}$ , which agrees well with the nominal one and that deduced from the crystal structure refinements.

Estimation of the oxygen content in the  $\text{Yb}_3\text{Pt}_4\text{Ge}_{13}$  sample was performed by EDXS and wave length dispersive X-ray analysis (WDXS) using a Jeol JSM 6610 scanning electron microscope equipped with an UltraDry EDS detector and Mag- naRay WDS spectrometer (ThermoFisher NSS7 system).

The element mapping based on the K- and L-lines X-ray intensities shows well defined  $\text{Yb}_2\text{O}_3$  particles and further minority phase  $\text{PtGe}_2$  (see Fig. 12). The  $\text{OK}_{\alpha}$  mapping with the WSi<sub>60</sub> monochromator crystal reveals no significant intensity at the majority phase  $\text{Yb}_3\text{Pt}_4\text{Ge}_{13}$ .

**Electronic structure calculations.** Scalar-relativistic electronic structures of  $\text{Ca}_3\text{Pt}_4\text{Ge}_{13}$  and  $\text{Yb}_3\text{Pt}_4\text{Ge}_{13}$  were calculated in the framework of density-functional theory (DFT) using the full-potential FPLO code (version 9.01–35) with the basis set of local orbitals.<sup>41</sup> The exchange-correlation potential by Perdew and Wang was applied.<sup>42</sup> The *k*-meshes included 120 points for  $\text{Yb}_3\text{Pt}_4\text{Ge}_{13}$  (80 atoms in the unit cell) and 32 points for

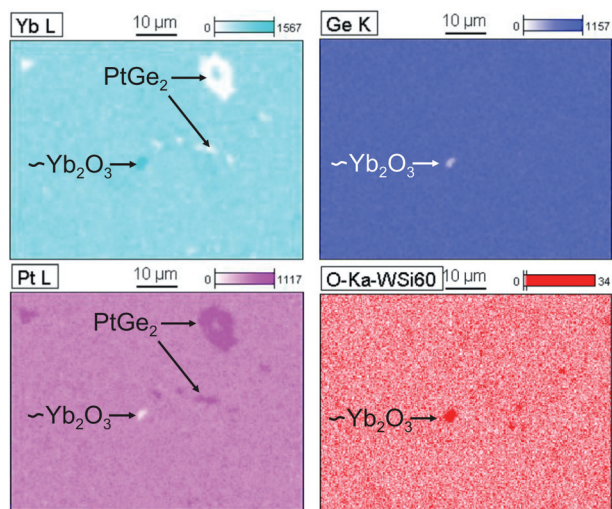


**Fig. 12** X-Ray intensity element mappings show the EDXS absolute counts of YbL, PtL and GeK lines. The WDXS intensity of  $OK\alpha$  line was measured with the WSi<sub>60</sub> spectrometer. The Yb<sub>3</sub>Pt<sub>4</sub>Ge<sub>13</sub> sample contains small grains of the minority phases PtGe<sub>2</sub> and Yb<sub>2</sub>O<sub>3</sub> (labelled in figure).

Ca<sub>3</sub>Pt<sub>4</sub>Ge<sub>13</sub> (160 atoms in the unit cell) in the symmetry-irreducible part of the first Brillouin zone. The calculation was done for the experimentally obtained model of Yb<sub>3</sub>Pt<sub>4</sub>Ge<sub>13</sub> and for the fully ordered model Ca<sub>3</sub>Pt<sub>4</sub>Ge<sub>13</sub>, with experimental lattice parameter and the Ge1 and Ge4 positions fully occupied, as well the T1 position occupied solely by Ge. In addition, the calculations were made for Ca<sub>3</sub>Pt<sub>4</sub>Ge<sub>13</sub> with a crystal structure of the Pr<sub>3</sub>Rh<sub>4</sub>Sn<sub>13</sub> type.

**Physical properties.** The magnetization of polycrystalline sample pieces was measured in a SQUID magnetometer (MPMS XL-7, Quantum Design) in external fields  $\mu_0 H$  between 2 mT and 7 T and temperatures between 1.8–400 K. The heat capacity measurements were performed with a relaxation-type calorimeter (PPMS, Quantum Design) in magnetic fields up to 9 T between 1.8 and 320 K. Electrical resistivity was determined with a low-frequency ac technique on a PPMS platform in zero and 9 T fields.

**X-Ray absorption spectroscopy (XAS) and resonant inelastic X-ray scattering (RIXS).** The experiments were performed at beamline ID26 of the European Synchrotron Radiation Facilities (ESRF) in Grenoble<sup>43</sup> on powdered samples (*ca.* 15 mg) diluted with B<sub>4</sub>C and embedded in paraffin wax. The incident energy was selected using the  $\langle 311 \rangle$  reflection of a double Si crystal monochromator. Rejection of higher harmonics was achieved by three Si mirrors at an angle of 2.5 mrad relative to the incident beam. The beam size was estimated to be  $\sim 0.3$  mm vertically and 1 mm horizontally. X-Ray absorption near-edge structure (XANES) spectra were measured in high energy resolution fluorescence detection (HERFD) mode using an X-ray emission spectrometer.<sup>44</sup> The sample, analyzer crystal and photon detector (avalanche photodiode) were arranged in a vertical Rowland geometry. The Yb HERFD spectra at the  $L_{III}$  edge were obtained by recording the maximum intensity of the Yb  $L\alpha_1$  emission line (7416 eV) as a function of the incident energy. The emission

energy was selected using the  $\langle 620 \rangle$  reflection of five spherically-bent Ge-crystal analyzers (with 1 m bending radius) aligned at 69° Bragg angle. The full core-to-valence resonant inelastic X-ray scattering (RIXS) plane around the Yb  $L_{III}$  edge was measured by scanning the incident energy at different emission energies. The emission energy in that case was selected using the  $\langle 800 \rangle$  reflection of two spherically-bent Ge-crystal analyzers aligned at 79° Bragg angle for the measurements of the Yb<sub>3</sub>Pt<sub>4</sub>Ge<sub>13</sub> sample and one crystal analyzer for the measurements of the Yb<sub>2</sub>O<sub>3</sub> sample. The intensity was normalized to the incident flux. A combined (incident convoluted with emitted) energy resolution of 1.2 and 1.4 eV was achieved in the HERFD and core-to-valence RIXS measurements, respectively.

## Acknowledgements

We are indebted to Yu. Prots for performing high-resolution X-ray diffraction measurements and helpful discussions. We thank P. Scheppan and S. Kostmann for metallographic and EDXS studies of the sample. The help of S. Leipe with high-pressure syntheses is gratefully acknowledged. A.T. was funded by Alexander von Humboldt Foundation.

## Notes and references

- 1 C. Uher, *Semicond. Semimet.*, 2001, **69**, 139.
- 2 B. C. Sales, in *Handbook on the Physics and Chemistry of Rare Earths*, ed. K. A. Gschneidner, Jr., J.-C. G. Bünzli and V. K. Pecharsky, Elsevier, Amsterdam, 2003, vol. 33, pp. 211, 1.
- 3 G. S. Nolas, D. T. Morelli and T. M. Tritt, *Annu. Rev. Mater. Sci.*, 1999, **29**, 89.
- 4 A. Leithe-Jasper, W. Schnelle, H. Rosner, N. Senthilkumaran, A. Rabis, M. Baenitz, A. Gippius, E. Morozova, J. A. Mydosh and Y. Grin, *Phys. Rev. Lett.*, 2003, **91**, 037208.
- 5 H. Zhang, H. Borrmann, N. Oeschler, C. Candolfi, W. Schnelle, M. Schmidt, U. Burkhardt, M. Baitinger, J. T. Zhao and Yu. Grin, *Inorg. Chem.*, 2011, **50**, 1250.
- 6 W. Carrillo-Cabrera, R. C. Gil, S. Paschen and Yu. Grin, *Z. Kristallogr. – New Cryst. Struct.*, 2002, **217**, 183.
- 7 K. H. Jack and V. Guttman, *Mater. Res. Bull.*, 1951, **4**, 246.
- 8 J. M. Vandenberg, *Mater. Res. Bull.*, 1980, **15**, 835.
- 9 R. Gumeniuk, W. Schnelle, H. Rosner, M. Nicklas, A. Leithe-Jasper and Yu. Grin, *Phys. Rev. Lett.*, 2008, **100**, 017002.
- 10 R. Gumeniuk, H. Borrmann, A. Ormeci, H. Rosner, W. Schnelle, M. Nicklas, Yu. Grin and A. Leithe-Jasper, *Z. Kristallogr.*, 2010, **225**, 531.
- 11 M. Shirogami, I. Shimaya, K. Kihou, C. Sekine and T. Yagi, *J. Solid State Chem.*, 2003, **174**, 32.
- 12 K. Kihou, I. Shirogami, Y. Shimaya, C. Sekine and T. Yagi, *Mater. Res. Bull.*, 2004, **39**, 317.
- 13 R. Gumeniuk, M. Schöneich, A. Leithe-Jasper, W. Schnelle, M. Nicklas, H. Rosner, A. Ormeci, U. Burkhardt, M. Schmidt, U. Schwarz, M. Ruck and Yu. Grin, *New J. Phys.*, 2010, **12**, 103035.
- 14 P. Villars, *Pearson's Handbook, Crystallographic Data for Intermetallic Phases*. Materials Park, OH 44073, 1997.
- 15 G. K. Shenoy, B. D. Dunlap and F. Y. Fradin, *Ternary Superconductors*, Elsevier, North-Holland, Amsterdam, 1981.
- 16 J. P. Remeika, G. P. Espinosa, A. S. Cooper, H. Barz, J. M. Rowell, D. B. McWahn, J. M. Vandenberg, D. E. Moncton, Z. Fisk, L. D. Woolf, H. C. Hamaker, M. B. Maple, G. Shirane and W. Thomlinson, *Solid State Commun.*, 1980, **34**, 923.
- 17 J. L. Hodeau, J. Chenavas, M. Marezio and J. P. Remeika, *Solid State Commun.*, 1980, **36**, 839.
- 18 Ya. Mudryk, A. Grytsiv, P. Rogl, C. Dusek, A. Galatanu, E. Idl, H. Michor, E. Bauer, C. Godart, D. Kaczorowski, L. Romaka and O. Bodak, *J. Phys. Condens. Matter*, 2001, **13**, 7391.
- 19 N. Kase, H. Hayamizu and J. Akimitsu, *Phys. Rev. B*, 2011, **83**, 184509.

- 20 D. Niepmann, R. Pöttgen, K. M. Poduska, F. J. DiSalvo, H. Trill and B. D. Mosel, *Z. Naturforsch. B*, 2001, **56**, 1.
- 21 P. Bordet, D. E. Cox, G. P. Espinosa, J. L. Hodeau and M. Marezio, *Solid State Commun.*, 1991, **78**, 359.
- 22 C. Nagoshi, R. Yamamoto, K. Kuwahara, H. Sagayama, D. Kawana, M. Kohgi, H. Sugawara, Y. Aoki, H. Sato, T. Yokoo and M. Arai, *J. Phys. Soc. Jpn.*, 2006, **75**, 044710.
- 23 S. Miraglia, J. L. Hodeau, M. Marezio, C. Laviron, M. Ghedira and G. P. Espinosa, *J. Solid State Chem.*, 1986, **63**, 358.
- 24 L. G. Akselrud and V. Davydov, *Visnyk Lviv. Univ. Ser. Khim.*, 2001, **39**, 112.
- 25 W. Jeitschko and D. Braun, *Acta Crystallogr., Sect. B: Struct. Crystallogr. Cryst. Chem.*, 1977, **33**, 3401.
- 26 A. Roushown and Y. Masatomo, *J. Solid State Chem.*, 2005, **178**, 2867.
- 27 M. O'Keeffe and B. G. Hyde, *Crystal Structures, Mineralogical Society of America*, BookCrafters, Inc., Chelsea, Michigan, USA, 1996.
- 28 Y. Liang, H. Borrmann, M. Baenitz, W. Schnelle, S. Budnyk, J. T. Zhao and Yu. Grin, *Inorg. Chem.*, 2008, **47**, 9489.
- 29 J. Emsley, *The Elements*, Oxford University Press, 1998.
- 30 P. I. Krypiakevych, *Structure Types of Intermetallic Compounds*, Nauka, Moscow, 1977.
- 31 L. Ben Farhat, M. Amami, E. K. Hlil and R. Ben Hassen, *J. Alloys Compd.*, 2009, **485**, 701.
- 32 W. Schnelle, A. Leithe-Jasper, H. Rosner, R. Cardoso-Gil, R. Gumeniuk, D. Trots, J. A. Mydosh and Y. Grin, *Phys. Rev. B*, 2008, **77**, 094421.
- 33 P. Glatzel, J. Singh, K. O. Kvashnina and J. A. van Bokhoven, *J. Am. Chem. Soc.*, 2010, **132**, 2555.
- 34 J. Jimenez-Mier, J. van Ek, D. L. Ederer, T. A. Callcott, J. J. Jia, J. Carlisle, L. Terminello, A. Asfaw and R. C. Perera, *Phys. Rev. B*, 1999, **59**, 2649.
- 35 J. C. Fuggle and J. E. Inglesfield, *Top. Appl. Phys.*, 1992, **69**, 1.
- 36 A. L. Ankudinov, B. Ravel, J. J. Rehr and S. D. Conradson, *Phys. Rev. B*, 1998, **58**, 7565.
- 37 D. Walker, M. A. Carpenter and C. M. Hitch, *Am. Mineral.*, 1990, **75**, 1020.
- 38 D. A. Young, *Phase Diagrams of the Elements*, University of California Press, Berkeley, CA, 1991.
- 39 M. J. Walter, Y. Thibault, K. Wei and R. W. Luth, *Can. J. Phys.*, 1995, **73**, 273.
- 40 L. G. Akselrud, P. Y. Zavali, Yu. N. Grin, V. K. Pecharsky, B. Baumgartner and E. Wölfel, *Mater. Sci. Forum*, 1993, **133–136**, 335.
- 41 K. Koepernik and H. Rosner, *Phys. Rev. B*, 1999, **59**, 1743.
- 42 J. P. Perdew and Y. Wang, *Phys. Rev. B*, 1992, **45**, 13244.
- 43 C. Gauthier, V. A. Sole, R. Signorato, J. Goulon and E. Moguiline, *J. Synchrotron Radiat.*, 1999, **6**, 164.
- 44 P. Glatzel and U. Bergmann, *Coord. Chem. Rev.*, 2005, **249**, 65.